

## A novel imaging measurement model for vision and inertial navigation fusion with extended Kalman filtering

Leandro R. Lustosa\* and Jacques Waldmann†

*Instituto Tecnológico de Aeronáutica, São José dos Campos, Brazil*

It is well-known that stand-alone inertial navigation systems (INS) have their errors diverging with time. The traditional approach for solving such inconvenience is to resort to position and velocity aiding such as global navigation satellite systems (GNSS) signals. However, misalignment errors in such fusion architecture are not observable in the absence of maneuvers. This investigation develops a novel sighting device (SD) model for vision-aided inertial navigation for use in psi-angle error based extended Kalman filtering by means of observations of *a priori* mapped landmarks. Additionally, the psi-angle error model is revisited and an extended Kalman filter datasheet-based tuning is explained. Results are obtained by computer simulation, where an unmanned aerial vehicle flies a known trajectory with inertial sensor measurements corrupted by a random constant model. Position and velocity errors, misalignment, accelerometer bias, rate-gyro drift and GNSS clock errors with respect to ground-truth are estimated by means of INS/GNSS/SD fusion and tested for statistical consistency.

### I. Introduction

Advances in microelectromechanical inertial sensors (MEMs) made low-cost inertial navigation systems (INS) commercially available. On the other hand, their errors quickly diverge with time and set an upper bound on the duration of autonomous operations and thus such systems become improper for use in low-cost unmanned aerial vehicle (UAV) missions. The traditional approach for solving such inconvenience is to resort to a global navigation satellite system (GNSS) receiver as position and velocity aiding device. Hence, INS/GNSS fusion yields bounded navigation errors. However, misalignment errors in such fusion architecture are not observable in the absence of maneuvers [1, 2]. In the light of such restriction, the present study develops a novel model for INS/GNSS and sighting device (SD) integration for use in outdoor navigation with known landmarks. In general, outdoor navigation in structured environments requires some sort of road-following. Herein, *a priori* mapped landmarks are imaged by a camera and tracked in the image plane to aid the INS.

An initial study on the matter was conducted in [3], which developed two distinct strategies for INS/SD fusion by means of psi-angle error model [4] based extended Kalman filtering (EKF). One of them is the inspiration for this paper and explores a relationship between the INS errors and the position of a landmark in the field of view relative to the line of sight (LOS) of the SD, after the latter is aimed at the assumed position of the landmark. The shortcoming of such procedure is the restriction to have the camera maintaining LOS pointing to the landmark. Such restriction has been recently overcome by means of resorting to a generalized SD model in which the difference between measured

---

\*M.Sc. Student, Department of Systems and Control, lustosa.leandro at gmail.com.

†Associate Professor, Department of Systems and Control, jacques at ita.br.

and estimated positions of the tracked landmark in the plane of image are correlated with INS errors [5].

However, the psi-angle error framework has received only a modicum of attention in INS/SD integration [6] since [3]. The present investigation revisits such scheme, which has proven successful for INS/GNSS fusion [7], by means of developing an INS/SD fusion formulation within the psi-angle error based EKF framework.

Initially, the INS psi-angle error model is revisited, and a datasheet-based nominal EKF tuning is explored alongside. Ultimately, an INS/GNSS/SD EKF-based fusion strategy is proposed for the estimation of navigation and sensors errors, and evaluated by means of Monte Carlo simulation and statistical consistency tests [8].

## II. Reference frames and Earth model

Reference frames and the Earth model are here briefly discussed. The WGS-84 ellipsoid has been used due to its accuracy and simplicity [9]. The local reference frames at the true and computed positions differ [4], and are respectively denoted by  $T = \{\hat{\mathbf{t}}_1, \hat{\mathbf{t}}_2, \hat{\mathbf{t}}_3\}$  and  $C = \{\hat{\mathbf{c}}_1, \hat{\mathbf{c}}_2, \hat{\mathbf{c}}_3\}$  (see figure 1).

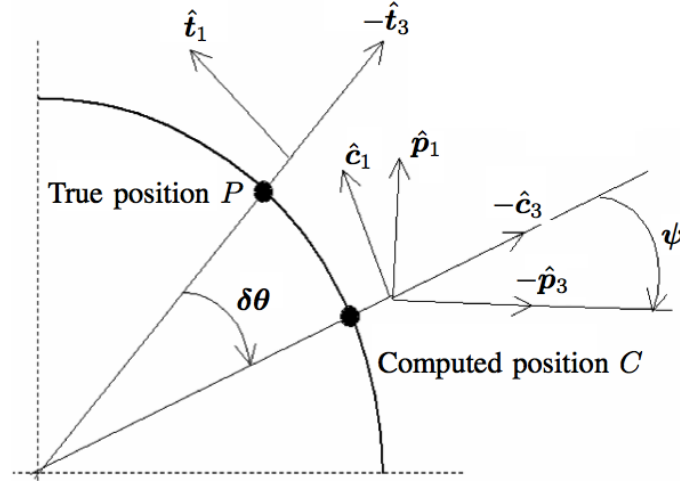


Figure 1. Illustration of true (P) and computed (C) positions; and platform (P), computed (C) and true (T) reference frames.

Additionally, equally important frames are  $I$ ,  $E$ ,  $B$  and  $P$ , respectively, inertial, Earth-fixed, vehicle body and platform coordinate systems. The latter is the local reference frame computed by the inertial navigation system at its estimated position and affected by attitude estimation errors [4].

## III. Mathematical notation

The chosen notation [10] is illustrated by table 1.

Furthermore, the decomposition of a vector  $\mathbf{v} \in \mathbb{R}^3$  into its components in a  $R$  coordinate system is denoted by means of the right subscript position, e.g.

$$\mathbf{v}_R = \begin{pmatrix} v_{r1} & v_{r2} & v_{r3} \end{pmatrix}^T \quad (1)$$

**Table 1. Kinematics notation**

Notation	Meaning
$\mathbf{p}^{X/Y}$	Position of point $X$ w.r.t. point $Y$
$\mathbf{R}$	INS position with respect to Earth centre
$\hat{\mathbf{R}}_{INS}$	INS-computed position with respect to Earth centre
$\overset{e}{\mathbf{R}} = \mathbf{v}$	Terrestrial velocity
$\overset{e}{\hat{\mathbf{R}}}_{INS} = \hat{\mathbf{v}}_{INS}$	INS-computed terrestrial velocity
$\overset{ss}{\mathbf{R}}$	Acceleration w.r.t. $S$ reference frame
$\boldsymbol{\omega}^{xy}$	Angular velocity of $X$ coordinate frame w.r.t. $Y$ frame
$\mathbf{A}_{sp}$	Specific force
$\mathbf{g}(\cdot)$	Earth gravity at designated point
$D_B^A$	Direction cosine matrix: rotates from $A$ coordinate frame into alignment with $B$ frame

#### IV. Kalman filter formulation

For the purpose of EKF-based INS/GNSS/SD fusion, the INS psi-angle error, GNSS receiver and camera linear models are outlined, i.e., linear state and covariance propagation and update are formulated.

##### A. INS psi-angle error model revisited

Consider strapdown accelerometers and rate-gyros measurements corrupted, respectively, by unknown constant bias  $\nabla$  and drift  $\epsilon$ , modelled as random normal variables with  $\sigma_\nabla$  and  $\sigma_\epsilon$  standard deviations. Additionally, additive zero-mean white additive noise  $\boldsymbol{\omega}_{accel}$  and  $\boldsymbol{\omega}_{gyro}$  are considered with  $\sigma_{accel}$  and  $\sigma_{gyro}$  standard deviations. The measured specific force  $\mathbf{A}_{sp,m}$  is given [4] by a rotation of  $\mathbf{A}_{sp}$  by the misalignment vector  $\boldsymbol{\psi}$  (see figure 1) from  $C$  to  $P$  reference frame, and biased by  $\nabla$  according to

$$\mathbf{A}_{sp,m} = \nabla + \mathbf{A}_{sp} - \boldsymbol{\psi} \times \mathbf{A}_{sp} + \boldsymbol{\omega}_{accel} \quad (2)$$

whereas [4]

$$\mathbf{A}_{sp} = \overset{ii}{\mathbf{R}} - \mathbf{g}(\mathbf{R}) - \boldsymbol{\Omega} \times (\boldsymbol{\Omega} \times \mathbf{R}) \quad (3)$$

and

$$\mathbf{A}_{sp,m} = \overset{ii}{\hat{\mathbf{R}}}_{INS} - \mathbf{g}(\hat{\mathbf{R}}_{INS}) - \boldsymbol{\Omega} \times (\boldsymbol{\Omega} \times \hat{\mathbf{R}}_{INS}) \quad (4)$$

where  $\boldsymbol{\psi}$ ,  $\mathbf{g}(\mathbf{R})$ ,  $\mathbf{g}(\hat{\mathbf{R}}_{INS})$ ,  $\boldsymbol{\Omega}$ ,  $\mathbf{R}$ ,  $\hat{\mathbf{R}}_{INS}$  denote, respectively, the misalignment rotation vector from the computed to the platform reference frame, Earth gravity at the true and computed positions, Earth angular velocity, and true and computed positions with respect to the Earth centre.

If  $\delta \mathbf{p}$  and  $\delta \mathbf{v}$  are defined as INS computed errors in position and velocity, i.e.,

$$\begin{cases} \delta \mathbf{p} = \hat{\mathbf{R}}_{INS} - \mathbf{R} \\ \delta \mathbf{v} = \hat{\mathbf{v}}_{INS} - \mathbf{v} \end{cases} \quad (5)$$

then equations 2, 3 and 4 imply

$$\nabla - \boldsymbol{\psi} \times \mathbf{A}_{sp} + \boldsymbol{\omega}_{accel} = \overset{ii}{\delta \mathbf{p}} - \underbrace{[g(\hat{\mathbf{R}}_{INS}) - g(\mathbf{R})]}_{\delta \mathbf{g}} - \boldsymbol{\Omega} \times (\boldsymbol{\Omega} \times \delta \mathbf{p}) \quad (6)$$

which can be rewritten as

$$\begin{aligned} \nabla - \boldsymbol{\psi} \times \mathbf{A}_{sp} + \boldsymbol{\omega}_{accel} &= \left( \overset{ie}{\delta \mathbf{p}} + \boldsymbol{\Omega} \times \overset{i}{\delta \mathbf{p}} \right) - \delta \mathbf{g} - \boldsymbol{\Omega} \times (\boldsymbol{\Omega} \times \delta \mathbf{p}) = \\ &= \overset{i}{\delta \mathbf{v}} + \boldsymbol{\Omega} \times \overset{i}{\delta \mathbf{p}} - \delta \mathbf{g} - \boldsymbol{\Omega} \times (\boldsymbol{\Omega} \times \delta \mathbf{p}) = \overset{c}{\delta \mathbf{v}} + \boldsymbol{\omega}^{ci} \times \delta \mathbf{v} + \boldsymbol{\Omega} \times \delta \mathbf{v} - \delta \mathbf{g} \end{aligned} \quad (7)$$

Ultimately,

$$\overset{c}{\delta \mathbf{v}} = \delta \mathbf{g} - (2\boldsymbol{\Omega} + \boldsymbol{\omega}^{ce}) \times \delta \mathbf{v} + \mathbf{A}_{sp} \times \boldsymbol{\psi} + \nabla + \boldsymbol{\omega}_{accel} \quad (8)$$

On the other hand, the derivative of  $\delta \mathbf{p}$  with respect to frame  $C$  yields

$$\overset{c}{\delta \mathbf{p}} = \overset{e}{\delta \mathbf{p}} - \boldsymbol{\omega}^{ce} \times \delta \mathbf{p} = \delta \mathbf{v} - \boldsymbol{\omega}^{ce} \times \delta \mathbf{p} \quad (9)$$

Additionally, it can be shown that [4]

$$\boldsymbol{\epsilon} = -\overset{i}{\boldsymbol{\psi}} - \boldsymbol{\omega}_{gyro} \quad (10)$$

hence

$$\overset{c}{\boldsymbol{\psi}} = \overset{i}{\boldsymbol{\psi}} - \boldsymbol{\omega}^{ci} \times \boldsymbol{\psi} = -\boldsymbol{\epsilon} - (\boldsymbol{\Omega} + \boldsymbol{\omega}^{ce}) \times \boldsymbol{\psi} - \boldsymbol{\omega}_{gyro} \quad (11)$$

Finally, according to [4], assuming  $\nabla_B$  and  $\boldsymbol{\epsilon}_B$  are random constants, representing vector equations 8, 9 and 11 in the  $C$  coordinate frame, and then employing the  $D_P^B$  estimated by the INS, the psi-angle-based INS error dynamics model is formulated as

$$\delta \dot{\mathbf{p}}_C = \delta \mathbf{v}_C - [\boldsymbol{\omega}_C^{ce} \times] \delta \mathbf{p}_C \quad (12)$$

$$\delta \dot{\mathbf{v}}_C = \delta \mathbf{g}_C - [(2\boldsymbol{\Omega}_C + \boldsymbol{\omega}_C^{ce}) \times] \delta \mathbf{v}_C + [D_P^B \mathbf{A}_{sp,m,B} \times] \boldsymbol{\psi}_C + D_P^B \nabla_B + D_P^B \boldsymbol{\omega}_{accel,B} \quad (13)$$

$$\dot{\boldsymbol{\psi}}_C = -[(\boldsymbol{\Omega}_C + \boldsymbol{\omega}_C^{ce}) \times] \boldsymbol{\psi}_C - D_P^B \boldsymbol{\epsilon}_B - D_P^B \boldsymbol{\omega}_{gyro,B} \quad (14)$$

$$\dot{\nabla}_B = \mathbf{0}_{3 \times 1} \quad (15)$$

$$\dot{\boldsymbol{\epsilon}}_B = \mathbf{0}_{3 \times 1} \quad (16)$$

where the notation  $[\boldsymbol{\zeta}_R \times]$  means

$$[\boldsymbol{\zeta}_R \times] = \begin{bmatrix} 0 & -\zeta_{r3} & \zeta_{r2} \\ \zeta_{r3} & 0 & -\zeta_{r1} \\ -\zeta_{r2} & \zeta_{r1} & 0 \end{bmatrix} \quad (17)$$

and  $\delta \mathbf{g}_C$  is approximated by [11]

$$\delta \mathbf{g}_C = \frac{g_e R_e^2}{(R_e + h_c)^3} \begin{pmatrix} -1 \\ -1 \\ 2 \end{pmatrix} \quad (18)$$

with  $g_e$  and  $R_e$  denoting, respectively, the gravity and the radius of the Earth as computed with the WGS-84 Earth model, at the geographic location of the INS sensors, according to [11]

$$R_e = R_0(1 - e \sin^2 \lambda_c) \quad (19)$$

and

$$g_e = (1 + 0.0053 \sin^2 \lambda_c) g_0 \quad (20)$$

where  $R_0$ ,  $e$ ,  $g_0$  and  $\lambda_c$  denote, respectively, the Earth equatorial radius, eccentricity and equatorial gravity, and the INS-computed latitude. The Earth model parameters are found in [9].

In the light of the foregoing development, it is convenient to define the EKF state vector as

$$\mathbf{x}_{EKF} = \left( \delta \mathbf{p}_C^T \quad \delta \mathbf{v}_C^T \quad \psi_C^T \quad \nabla_B^T \quad \epsilon_B^T \quad c\Delta t \right)^T \quad (21)$$

where  $c\Delta t$  denotes the random constant GNSS clock error model with  $\sigma_{c\Delta t}$  standard deviation, whose compensation is fundamental in INS/GNSS integration [11].

The zero-order hold (ZOH) discretization of equations 12, 13, 14, 15 and 16 yields the error-state transition matrix  $F_k$  and process noise covariance  $Q_k$  for the EKF. In practice, the discretization which yields  $Q_k$  is [12]

$$Q_k = G_k \begin{bmatrix} \sigma_{accel}^2 I_{3 \times 3} & 0_{3 \times 3} \\ 0_{3 \times 3} & \sigma_{gyro}^2 I_{3 \times 3} \end{bmatrix} \Delta t G_k^T \quad (22)$$

where

$$G_k = \begin{bmatrix} 0_{3 \times 3} & 0_{3 \times 3} \\ D_P^B & 0_{3 \times 3} \\ 0_{3 \times 3} & -D_P^B \\ 0_{7 \times 3} & 0_{7 \times 3} \end{bmatrix} \quad (23)$$

and  $\Delta t$  denotes the discretization sample time. Finally, EKF tuning is addressed with inertial sensors' datasheet specifications.

## B. GNSS tightly coupled integration

GNSS integration equations are listed in the following without further explanations due to the broad extension of available literature on the matter [7]. Integration is performed in a tightly coupled architecture involving pseudorange and deltarange measurements. For each satellite  $S_i$ , pseudorange and deltarange innovations are incorporated by means of equations 24 and 25, where  $\hat{\mathbf{u}}_i$  denotes the estimated line-of-sight (LOS) unit vector from the user's receiver antenna to satellite  $S_i$ . Pseudorange and deltarange measurements are corrupted by additive Gaussian noise  $\omega_{S_i,p} \sim N(0, \sigma_p)$  and  $\omega_{S_i,v} \sim N(0, \sigma_v)$ . The antenna lever arm has been considered as exactly compensated. Furthermore, GNSS clock error dynamics is modelled according to equation 26. In practice, a more complex model that

accounts for clock drift should be implemented [7]. However, for the sake of simplicity, the present work implements a simpler model and focuses on camera integration.

$$\mathbf{p}^{S_i/P} - \mathbf{p}^{S_i/C} = \hat{\mathbf{u}}_i \cdot \delta \mathbf{p} + c\Delta t + \boldsymbol{\omega}_{S_i,p} \quad (24)$$

$$\mathbf{\hat{p}}^{e^{S_i/P}} - \mathbf{\hat{p}}^{e^{S_i/C}} = \hat{\mathbf{u}}_i \cdot \delta \mathbf{v} + \boldsymbol{\omega}_{S_i,v} \quad (25)$$

$$\frac{d}{dt} c\Delta t = 0 \quad (26)$$

### C. Sighting device

As previously stated, the basic idea of the proposed INS/SD fusion architecture is based upon tracking mapped landmarks  $L_i \in L, i = 1..N_l$ , each one with *a priori* known LLA coordinates (latitude, longitude, altitude). For each  $L_i$ , its position with respect to the camera  $V$ ,  $\mathbf{p}^{L_i/V}$ , (see figure 2) is described in the  $V$  coordinate frame as [5]

$$\mathbf{p}_V^{L_i/V} = D_V^B [D_B^T D_T^E (\mathbf{p}_E^{L_i} - \mathbf{p}_E^P) - \mathbf{p}_B^{V/P}] \quad (27)$$

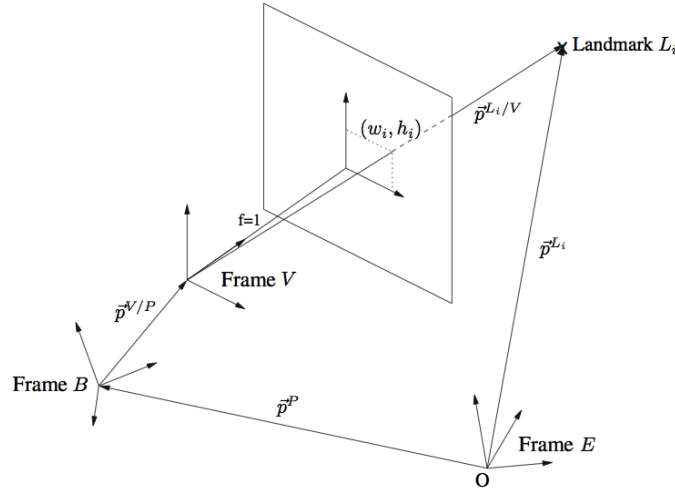


**Figure 2. Perspective projection geometry in the plane of image. Adapted from [5].**

The camera  $V$  is assumed installed next to the inertial sensors' position  $P$  and has its axes aligned according to figure 3, thus

$$\mathbf{p}_V^{L_i/V} = D_V^B D_B^T D_T^E (\mathbf{p}_E^{L_i} - \mathbf{p}_E^P) \quad (28)$$

Hence the adimensional normalized measurement<sup>a</sup>  $\mathbf{z}_{L_i} = (w_i, h_i)$  provided by the camera is given by

$$\mathbf{z}_{L_i} = \Pi \frac{\mathbf{p}_V^{L_i/V}}{\begin{bmatrix} 1 & 0 & 0 \end{bmatrix} \cdot \mathbf{p}_V^{L_i/V}} + \boldsymbol{\omega}_{cam} \quad (29)$$

<sup>a</sup>It is assumed, without loss of generality, camera focal length  $f = 1$ .

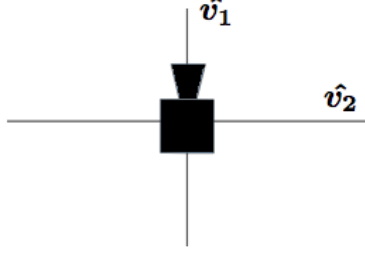


**Figure 3. Definition of camera coordinate system (top view).**

where  $\omega_{cam} \in M(\mathbb{R})_{2 \times 1}$  is white gaussian noise with standard deviation  $\sigma_{cam}$ , and  $\Pi$  is defined by

$$\Pi = \begin{bmatrix} 0 & 1 & 0 \\ 0 & 0 & 1 \end{bmatrix} \quad (30)$$

$\omega_{cam}$  shall be modelled to account for uncertainties in target tracking algorithms, servomechanism control and misalignment between camera and vehicle body<sup>b</sup>. The estimated normalized measurement vector is estimated by means of the navigation algorithm [13] computed variables (i.e., position, velocity and attitude) by

$$\hat{\mathbf{z}}_{L_i} = \Pi \frac{\mathbf{p}_{V_c}^{L_i/C}}{\begin{bmatrix} 1 & 0 & 0 \end{bmatrix} \cdot \mathbf{p}_{V_c}^{L_i/C}} \quad (31)$$

where  $V_c$  is the computed camera reference frame. Similarly to equation 28,  $\mathbf{p}_{V_c}^{L_i/C}$  is expressed as

$$\mathbf{p}_{V_c}^{L_i/C} = D_{V_c}^{B_c} D_{B_c}^C D_C^E (\mathbf{p}_E^{L_i} - \mathbf{p}_E^C) \quad (32)$$

The orientation of the camera  $V$  in relation to the vehicle body  $B$  is assumed known with great accuracy, thus  $D_{B_c}^{V_c} = D_B^V$ . In addition, notice that INS attitude estimates are employed and thus follows the approximation  $D_C^{B_c} \approx D_P^B$ . In this scope, equation 32 can be rewritten as

$$\mathbf{p}_{V_c}^{L_i/C} = D_V^B D_B^P D_C^E (\mathbf{p}_E^{L_i} - \mathbf{p}_E^C) \quad (33)$$

Notice that all terms in the right-hand side of equation 33 are available from INS navigation algorithm and  $\hat{\mathbf{z}}_{L_i}$  can be readily computed. For use in the EKF, the difference  $\mathbf{r}_{L_i} = \mathbf{z}_{L_i} - \hat{\mathbf{z}}_{L_i}$ , and how it relates to navigation errors, is explored in the following.

It has been assumed that  $\mathbf{r}_{L_i}$  is function solely of  $\delta \mathbf{p}$  and  $\psi$ , disregarding electrooptical distortions in the sighting device. Hence, the Jacobian  $J = \frac{\partial \mathbf{r}_{L_i}}{\partial \mathbf{x}}$  is in the sparse form

$$J = - \begin{bmatrix} \frac{\partial \hat{\mathbf{z}}_{L_i}}{\partial \delta \mathbf{p}_C} & 0_{2 \times 3} & \frac{\partial \hat{\mathbf{z}}_{L_i}}{\partial \psi_C} & 0_{2 \times 7} \end{bmatrix} \quad (34)$$

---

<sup>b</sup>Servomechanism control and misalignment between camera and vehicle body errors usually cannot be accurately modelled as white gaussian noise hence inflation in Kalman filter noise covariance statistics should take place in practice

First,  $\frac{\partial \hat{z}_{L_i}}{\partial \delta \mathbf{p}_C}$  is calculated noticing that equation 33 can be rewritten as

$$\begin{aligned}
\mathbf{p}_{V_C}^{L_i/C} &= D_V^B D_B^P D_C^E (\mathbf{p}_E^{L_i} - \mathbf{p}_E^C) = D_V^B (D_B^T D_T^C D_C^P) (D_C^T D_T^E) (\mathbf{p}_E^{L_i} - \mathbf{p}_E^C) \approx \\
&\approx D_V^B D_B^T (I_{3 \times 3} + [\boldsymbol{\psi}_C \times]) D_T^E (\mathbf{p}_E^{L_i} - \mathbf{p}_E^C) = D_V^B D_B^T (I_{3 \times 3} + [\boldsymbol{\psi}_C \times]) D_T^E (\mathbf{p}_E^{L_i} - \mathbf{p}_E^P - \boldsymbol{\delta} \mathbf{p}_E) = \\
&= D_V^B D_B^T D_T^E (\mathbf{p}_E^{L_i} - \mathbf{p}_E^P) + D_V^B D_B^T [\boldsymbol{\psi}_C \times] D_T^E (\mathbf{p}_E^{L_i} - \mathbf{p}_E^P) - D_V^B D_B^T (I_{3 \times 3} + [\boldsymbol{\psi}_C \times]) D_T^E D_C^E \boldsymbol{\delta} \mathbf{p}_C \approx \\
&\approx \mathbf{p}_V^{L_i/V} + D_V^B D_B^T [\boldsymbol{\psi}_C \times] D_T^E (\mathbf{p}_E^{L_i} - \mathbf{p}_E^P) - D_V^B D_B^T (I_{3 \times 3} + [\boldsymbol{\delta} \boldsymbol{\theta}_C \times]) \boldsymbol{\delta} \mathbf{p}_C \approx \\
&\approx \mathbf{p}_V^{L_i/V} + D_V^B D_B^T [\boldsymbol{\psi}_C \times] D_T^E (\mathbf{p}_E^{L_i} - \mathbf{p}_E^P) - D_V^B D_B^T \boldsymbol{\delta} \mathbf{p}_C \quad (35)
\end{aligned}$$

Therefore, considering the partial derivative  $\frac{\partial \hat{z}_{L_i}}{\partial \delta \mathbf{p}_C}$  at point  $\boldsymbol{\psi}_C = \mathbf{0}$ , above equations deliver

$$\mathbf{p}_{V_C}^{L_i/C} = \mathbf{p}_V^{L_i/V} - D_V^B D_B^T \boldsymbol{\delta} \mathbf{p}_C \quad (36)$$

For the computation of  $\frac{\partial \hat{z}_{L_i}}{\partial \mathbf{p}_C}$ ,  $\hat{z}_{L_i}$  is rewritten as

$$\hat{z}_{L_i} = \begin{pmatrix} z_1 \\ z_2 \end{pmatrix}, \quad z_1 = \frac{z_{1,num}}{z_{den}}, \quad \frac{z_{2,num}}{z_{den}} \quad (37)$$

$$z_{1,num} = \begin{bmatrix} 0 & 1 & 0 \end{bmatrix} (\mathbf{p}_V^{L_i/V} - D_V^B D_B^T \boldsymbol{\delta} \mathbf{p}_C) \quad (38)$$

$$z_{2,num} = \begin{bmatrix} 0 & 0 & 1 \end{bmatrix} (\mathbf{p}_V^{L_i/V} - D_V^B D_B^T \boldsymbol{\delta} \mathbf{p}_C) \quad (39)$$

$$z_{den} = \begin{bmatrix} 1 & 0 & 0 \end{bmatrix} (\mathbf{p}_V^{L_i/V} - D_V^B D_B^T \boldsymbol{\delta} \mathbf{p}_C) \quad (40)$$

Hence,

$$\frac{\partial \hat{z}_{L_i}}{\partial \delta \mathbf{p}_C} = \begin{bmatrix} \frac{\partial z_1}{\partial \delta p_{c1}} & \frac{\partial z_1}{\partial \delta p_{c2}} & \frac{\partial z_1}{\partial \delta p_{c3}} \\ \frac{\partial z_2}{\partial \delta p_{c1}} & \frac{\partial z_2}{\partial \delta p_{c2}} & \frac{\partial z_2}{\partial \delta p_{c3}} \end{bmatrix} \quad (41)$$

where

$$\frac{\partial z_k}{\partial \delta p_{cj}} = \frac{1}{z_{den}^2} \left( z_{den} \frac{\partial z_{k,num}}{\partial \delta p_{cj}} - z_{k,num} \frac{\partial z_{den}}{\partial \delta p_{cj}} \right), \quad \begin{matrix} k = 1..2 \\ j = 1..3 \end{matrix} \quad (42)$$

and

$$\begin{pmatrix} \frac{\partial z_{1,num}}{\partial \delta p_{c1}} \\ \frac{\partial z_{2,num}}{\partial \delta p_{c1}} \\ \frac{\partial z_{den}}{\partial \delta p_{c1}} \end{pmatrix} = - \begin{bmatrix} 0 & 1 & 0 \\ 0 & 0 & 1 \\ 1 & 0 & 0 \end{bmatrix} D_V^B D_B^T \begin{bmatrix} 1 \\ 0 \\ 0 \end{bmatrix} \quad (43)$$

$$\begin{pmatrix} \frac{\partial z_{1,num}}{\partial \delta p_{c2}} \\ \frac{\partial z_{2,num}}{\partial \delta p_{c2}} \\ \frac{\partial z_{den}}{\partial \delta p_{c2}} \end{pmatrix} = - \begin{bmatrix} 0 & 1 & 0 \\ 0 & 0 & 1 \\ 1 & 0 & 0 \end{bmatrix} D_V^B D_B^T \begin{bmatrix} 0 \\ 1 \\ 0 \end{bmatrix} \quad (44)$$

$$\begin{pmatrix} \frac{\partial z_{1,num}}{\partial \delta p_{c3}} \\ \frac{\partial z_{2,num}}{\partial \delta p_{c3}} \\ \frac{\partial z_{den}}{\partial \delta p_{c3}} \end{pmatrix} = - \begin{bmatrix} 0 & 1 & 0 \\ 0 & 0 & 1 \\ 1 & 0 & 0 \end{bmatrix} D_V^B D_B^T \begin{bmatrix} 0 \\ 0 \\ 1 \end{bmatrix} \quad (45)$$

Above computations deliver the first  $2 \times 3$  block of the Jacobian in equation 34. Similarly, for the computation of the remaining nonzero block, notice that the  $\boldsymbol{\psi}$  misalignment affects the camera measurement (for small angles) according to

$$\mathbf{p}_{V_C}^{L_i/C} = \mathbf{p}_V^{L_i/V} + D_V^B D_B^T [\boldsymbol{\psi}_C \times] D_T^E (\mathbf{p}_E^{L_i} - \mathbf{p}_E^P) \quad (46)$$



By means of equation 46 and the same strategy used for the computation of the Jacobian with respect to position, follows

$$\hat{\mathbf{z}}_{L_i} = \begin{pmatrix} \gamma_1 \\ \gamma_2 \end{pmatrix}, \quad \gamma_1 = \frac{\gamma_{1,num}}{\gamma_{den}}, \quad \gamma_2 = \frac{\gamma_{2,num}}{\gamma_{den}} \quad (47)$$

$$\gamma_{1,num} = \begin{bmatrix} 0 & 1 & 0 \end{bmatrix} (\mathbf{p}_V^{L_i/V} + D_V^B D_B^T [\boldsymbol{\psi}_C \times] D_T^E (\mathbf{p}_E^{L_i} - \mathbf{p}_E^P)) \quad (48)$$

$$\gamma_{2,num} = \begin{bmatrix} 0 & 0 & 1 \end{bmatrix} (\mathbf{p}_V^{L_i/V} + D_V^B D_B^T [\boldsymbol{\psi}_C \times] D_T^E (\mathbf{p}_E^{L_i} - \mathbf{p}_E^P)) \quad (49)$$

$$\gamma_{den} = \begin{bmatrix} 1 & 0 & 0 \end{bmatrix} (\mathbf{p}_V^{L_i/V} + D_V^B D_B^T [\boldsymbol{\psi}_C \times] D_T^E (\mathbf{p}_E^{L_i} - \mathbf{p}_E^P)) \quad (50)$$

$$\frac{\partial \hat{\mathbf{z}}_{L_i}}{\partial \boldsymbol{\psi}_C} = \begin{bmatrix} \frac{\partial \gamma_1}{\partial \psi_{c1}} & \frac{\partial \gamma_1}{\partial \psi_{c2}} & \frac{\partial \gamma_1}{\partial \psi_{c3}} \\ \frac{\partial \gamma_2}{\partial \psi_{c1}} & \frac{\partial \gamma_2}{\partial \psi_{c2}} & \frac{\partial \gamma_2}{\partial \psi_{c3}} \end{bmatrix} \quad (51)$$

$$\frac{\partial \gamma_k}{\partial \psi_{cj}} = \frac{1}{\gamma_{den}^2} \left( \gamma_{den} \frac{\partial \gamma_{k,num}}{\partial \psi_{cj}} - \gamma_{k,num} \frac{\partial \gamma_{den}}{\partial \psi_{cj}} \right), \quad \begin{matrix} k = 1..2 \\ j = 1..3 \end{matrix} \quad (52)$$

$$\begin{pmatrix} \frac{\partial \gamma_{1,num}}{\partial \psi_{c1}} \\ \frac{\partial \gamma_{2,num}}{\partial \psi_{c1}} \\ \frac{\partial \gamma_{den}}{\partial \psi_{c1}} \end{pmatrix} = \begin{bmatrix} 0 & 1 & 0 \\ 0 & 0 & 1 \\ 1 & 0 & 0 \end{bmatrix} D_V^B D_B^P \begin{bmatrix} 0 & 0 & 0 \\ 0 & 0 & -1 \\ 0 & 1 & 0 \end{bmatrix} D_C^E \mathbf{p}_E^{L_i/C} \quad (53)$$

$$\begin{pmatrix} \frac{\partial \gamma_{1,num}}{\partial \psi_{c2}} \\ \frac{\partial \gamma_{2,num}}{\partial \psi_{c2}} \\ \frac{\partial \gamma_{den}}{\partial \psi_{c2}} \end{pmatrix} = \begin{bmatrix} 0 & 1 & 0 \\ 0 & 0 & 1 \\ 1 & 0 & 0 \end{bmatrix} D_V^B D_B^P \begin{bmatrix} 0 & 0 & 1 \\ 0 & 0 & 0 \\ -1 & 0 & 0 \end{bmatrix} D_C^E \mathbf{p}_E^{L_i/C} \quad (54)$$

$$\begin{pmatrix} \frac{\partial \gamma_{1,num}}{\partial \psi_{c3}} \\ \frac{\partial \gamma_{2,num}}{\partial \psi_{c3}} \\ \frac{\partial \gamma_{den}}{\partial \psi_{c3}} \end{pmatrix} = \begin{bmatrix} 0 & 1 & 0 \\ 0 & 0 & 1 \\ 1 & 0 & 0 \end{bmatrix} D_V^B D_B^P \begin{bmatrix} 0 & -1 & 0 \\ 1 & 0 & 0 \\ 0 & 0 & 0 \end{bmatrix} D_C^E \mathbf{p}_E^{L_i/C} \quad (55)$$

Above computations deliver the Jacobian  $J$  which quantitatively describes how navigation errors affect camera pointing and is used as sensor model in the extended Kalman filter.

$$\mathbf{r}_{L_i} = J \mathbf{x}_{EKF} + \boldsymbol{\omega}_{cam} \quad (56)$$

## V. Simulation results

Consider a simulated scenario where an unmanned aerial vehicle (UAV), initially positioned at  $LLA = (0, 0, 100m)$ , equipped with 3-axis sensitive triads of strapdown rate-gyros and accelerometers, a GNSS receiver and a camera flies a trajectory with cruising speed  $300m/s$  toward North and altitude  $100m$ . Sensors specifications are illustrated by table 2.

GNSS/SD updates were made at  $100ms$  intervals. After the instant  $t = 5sec$ , EKF estimated navigation variables and sensors errors are used for in-flight correction of the INS computed position, velocity and attitude and to calibrate the inertial sensors and GNSS receiver clock error. INS correction is of utmost importance in such systems due to the linearization of the INS error dynamics at the computed INS navigation solution.

**Table 2. Sensors Imperfections**

INS	$\sigma_{accel}$ $1mg$	$\sigma_{\nabla}$ $25mg$	$\sigma_{gyro}$ $1^\circ/h$	$\sigma_{\epsilon}$ $25^\circ/h$
GNSS/SD	$\sigma_{c\Delta t}$ $300m$	$\sigma_v$ $0.01m/s$	$\sigma_p$ $15m$	$\sigma_{cam}$ $0.01$

With respect to the INS navigation algorithm, [13] and [14] provide cost-effective multiple-rate integration methods to compute position and velocity, and attitude, respectively. However, such algorithms incur in errors in position, velocity and attitude, commonly known in the literature as scrolling, sculling [16] and coning [15]. Scrolling errors added to the position channel process noise (see equation 22) precludes EKF optimality, and hence *ad-hoc*  $Q_k$  inflation takes place in the following manner

$$Q_k \leftarrow Q_k + 10^{-1} \Delta t \begin{bmatrix} I_{3 \times 3} & 0_{3 \times 13} \\ 0_{13 \times 3} & 0_{13 \times 13} \end{bmatrix} \quad (57)$$

On top of that, the initial extended Kalman filter covariance matrix  $P(0|0)$  is also inflated. Such procedure is commonplace in real applications since initial errors are often not known. This practice yields a non-optimal pessimist filter initiation which can be detected by substantial differences in root mean squared (RMS) estimation and EKF computed covariance during the KF's early working stages as can be seen later on.

The impact of the number of available landmarks on INS/GNSS/SD system performance will be evaluated by comparing single-sided and double-sided observation scenarios. Only one landmark update is made at each updating step of the EKF. In the case of single-sided observations, only landmark  $L_1$  is considered in the filter update. In the double-sided observation mode,  $L_1$  and  $L_2$  are alternately available for the update stage. Landmarks are defined in table 3. The vehicle's trajectory and the observed landmarks are illustrated in figure 4.

**Table 3. Landmarks Position Coordinates**

Landmark	Latitude ( $deg$ )	Longitude ( $deg$ )	Altitude ( $m$ )
1	$10^{-2}$	$50 \times 10^{-1}$	10
2	$50 \times 10^{-1}$	$10^{-2}$	10

For the sake of simplicity, constant visibility to 4 GNSS satellites is assumed, each with a fixed position with respect to Earth during the simulation time interval. LLA satellite coordinates are given in table 4.

The evaluation of INS/GNSS/SD fusion algorithm performance with single or double-sided observations is based on a Monte Carlo simulation [8] with 50 realizations and two statistical tests. These are the normalized estimation error squared (NEES) and normalized innovation squared (NIS), which are described in [8] and used hereafter with a 5% alarm rate. The number of realizations is chosen so that a balance between reliable statistical study and practicable simulation time is obtained.

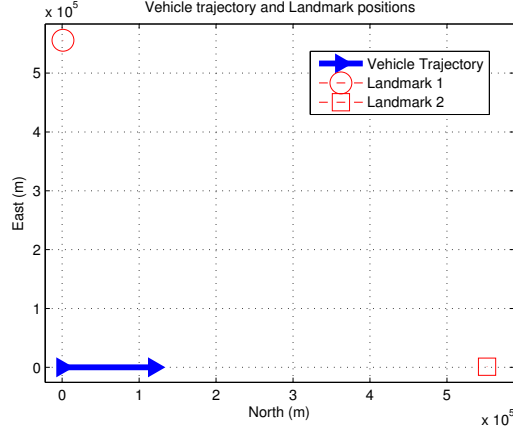


Figure 4. Vehicle trajectory and landmark positions (top view).

Table 4. GNSS Satellites Position Coordinates

Satellite	Latitude ( $deg$ )	Longitude ( $deg$ )	Altitude ( $km$ )
1	20	-20	20,000
2	40	-20	20,000
3	-30	40	20,000
4	-25	30	20,000

### A. Single-sided observations

Figure 5 displays INS/GNSS/SD fusion with single-sided observations EKF computed covariances and root mean squared (RMS) estimation errors (denoted by  $\delta\tilde{\mathbf{p}}$ ,  $\delta\tilde{\mathbf{v}}$ ,  $\tilde{\psi}$ ,  $\tilde{\nabla}$ ,  $\tilde{\epsilon}$  and  $c\Delta\tilde{t}$ ) for each component of  $\mathbf{x}_{EKF}$ . Additionally, NEES and NIS consistency tests are shown with the corresponding alarm limits.

Notice, in sharp contrast with INS/GNSS fusion, the observability of  $\psi_{c1}$  and  $\psi_{c3}$  without resorting to maneuvers. Notwithstanding,  $\psi_{c2}$  is weakly observable due to landmark  $L_1$  location East of the vehicle. It is, indeed, intuitive to expect the inadequacy of sighting devices to yield attitude information about the LOS axis due to the assumed punctual nature of the landmark projection on the image plane. Similarly,  $\nabla_{b1}$  is weakly observable.

### B. Double-sided observations

Figure 6 displays INS/GNSS/SD fusion with double-sided observations EKF computed covariances and RMS estimation errors for each component of  $\mathbf{x}_{EKF}$ . Additionally, NEES and NIS consistency tests are shown with the corresponding alarm limits.

The addition of a geometrically favorable landmark, namely  $L_2$ , positioned North of the vehicle, enhances  $\psi_{c2}$  and  $\nabla_{b1}$  observability. Thus, the RMS error quickly diminishes and filter tuning is accomplished as far as the NEES and NIS tests can evaluate.

Furthermore, this work suggests as future work further investigation on the impact of number and geometry of landmarks on Kalman filter observability, which can be analytically performed in a fashion similar to [1, 2].

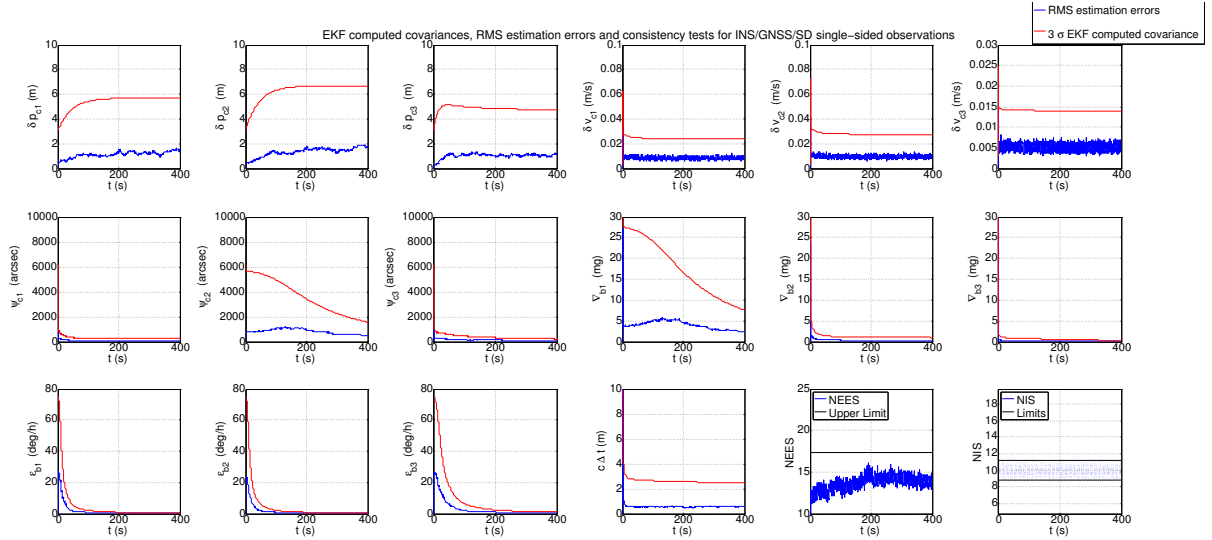


Figure 5. EKF computed covariances, RMS estimation errors and consistency tests for INS/GNSS/SD single-sided observations.

As a last remark, the EKF process noise in the position channel must be inflated according to equation 57 to accomplish NEES and NIS statistical consistency. Otherwise, the resulting small EKF computed covariance and the corresponding RMS error become statistically inconsistent, which may render the estimation process unreliable. The tuning of the position channel noise to reach statistical consistency in the NEES test can be addressed by self-tuning algorithms [17, 18].

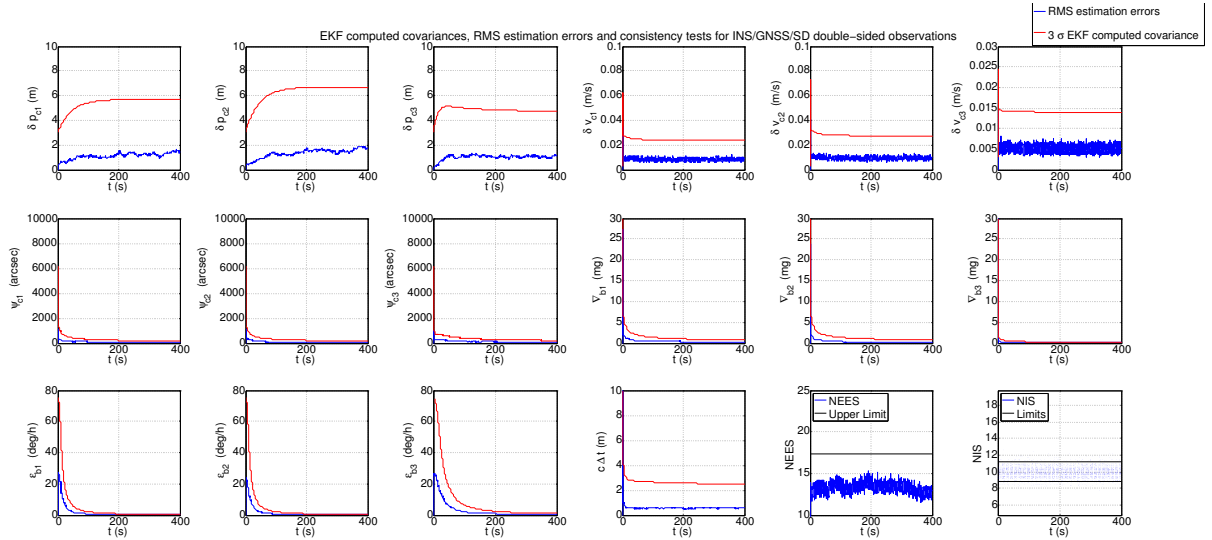


Figure 6. EKF computed covariances, RMS estimation errors and consistency tests for INS/GNSS/SD double-sided observations.

## VI. Conclusions

An imaging measurement model is formulated for use in a psi-angle error based extended Kalman filter (EKF) that yields the fusion of global navigation satellite observ-

ables with vision-aided inertial navigation. At first, the EKF uses datasheet-based nominal tuning and the estimation performance is evaluated by means of Monte Carlo simulation. The resulting performance motivates the use of a process noise inflation scheme to attain statistical consistency. Position and velocity errors, misalignment, accelerometer bias, rate-gyro drift and GNSS clock errors with respect to ground-truth are then effectively estimated and pass the tests for statistical consistency. Ultimately, in-flight INS correction and the calibration of inertial sensors and GNSS receiver clock error are successfully accomplished.

### Acknowledgments

This material is based upon research supported by project FINEP/SIA 11382\*2, conducted at SIA Lab, Department of Systems and Control, Faculty of Electronics and Computer Engineering, Instituto Tecnológico de Aeronáutica - ITA, São José dos Campos - SP, Brazil

### References

- [1] D. Goshen-Meskin, I. Y. Bar-Itzhack, Observability analysis of piece-wise constant systems with application to inertial navigation. In: Proc. 29th IEEE Conf. Decision and Control. 1990. p. 821–826.
- [2] D. Goshen-Meskin, I. Y. Bar-Itzhack, Observability analysis of piece-wise constant systems. ii. application to inertial navigation in-flight alignment [military applications]. IEEE Trans. Aerospace and Electronic Systems, v. 28, n. 4, p. 1068–1075, 1992.
- [3] I. Y. Bar-Itzhack, Optimal updating of INS using sighting devices. Journal of Guidance and Control, v. 1, n. 5, p. 305–313, 1978.
- [4] A. Weinred, I. Y. Bar-Itzhack, The psi-angle error equation in strapdown inertial navigation systems. IEEE Trans. Aerospace and Electronic Systems, AES-14, n. 3, p. 539–542, 1978.
- [5] N. Trawny, A. I. Mourikis, S. I. Roumeliotis, A. E. Johnson, J. Montgomery, Vision-aided inertial navigation for pin-point landing using observations of mapped landmarks. Journal of Field Robotics, v. 24, n. 5, p. 357–378, 2007.
- [6] J. Wang, M. Garratt, A. Lambert, J. J. Wang, S. Han, D. Sinclair, Integration of GPS/INS/vision sensors to navigate unmanned aerial vehicles. In: IAPRS&SIS. Beijing, China. 2008. v. 37, p. 963–969.
- [7] J. A. Farrell, M. Barth, The Global Positioning System and Inertial Navigation. McGraw-Hill, 1998.
- [8] Y. Bar-Shalom, X. R. Li, T. Kirubarajan, Estimation with Applications to Tracking and Navigation - Theory Algorithms and Software. Wiley, 2001.
- [9] National Imagery and Mapping Agency, Technical Report TR8350.2 Department of Defense World Geodetic System 1984, Its Definitions and Relationships with Local Geodetic Systems. 3. ed. 2000.

- [10] R. A. Tenenbaum, Fundamentals of Applied Dynamics, Springer, 2004.
- [11] G. R. Pitman (ed.), Inertial Guidance, Wiley, New York, 1962.
- [12] P. S. Maybeck, Stochastic Models, Estimation, and Control. Academic Press, 1979.
- [13] I. Y. Bar-Itzhack, Navigation computation in terrestrial strapdown inertial navigation systems. IEEE Transactions on Aerospace and Electronic Systems, n. 6, p. 679–689, 1977.
- [14] O. S. Salychev, Applied Inertial Navigation: Problems and Solutions. BMSTU Press, 2004.
- [15] P. G. Savage, Strapdown inertial navigation integration algorithm design, Part 1: Attitude algorithms. Journal of Guidance, Control, and Dynamics, v. 21, n. 1, p. 19–28, January-February 1998.
- [16] P. G. Savage, Strapdown inertial navigation integration algorithm design, Part 2: Velocity and position algorithms. Journal of Guidance, Control, and Dynamics, v. 21, n. 2, p. 208–221, March-April 1998.
- [17] L. R. Lustosa, J. Waldmann, Addressing the statistical consistency of extended Kalman filtering for aided inertial navigation using adaptive techniques. In: Proceedings of 19th Saint Petersburg International Conference on Integrated Navigation Systems. Saint Petersburg, Russia. May 2012.
- [18] L. R. Lustosa, Sintonia automática de filtro de Kalman para navegação inercial auxiliada. M.Sc. thesis. Instituto Tecnológico de Aeronáutica - ITA, Brazil, 2012.